Bioinspired crystallization, sensitized luminescence and cytocompatibility of citrate-functionalized Ca-substituted europium phosphate monohydrate nanophosphors

Jaime Gómez-Morales [a,*], Cristóbal Verdugo-Escamilla [a], Raquel Fernández-Penas [a], Carmen Maria Parra-Milla [a], Christophe Drouet [b,c], Michele Iafisco [c], Francesca Oltolina [d], Maria Prat [d], Jorge Fernando Fernández-Sánchez [e]

[a] Laboratorio de Estudios Cristalográficos, IACT, CSIC-UGR Avda. Las Palmeras, n° 4, E-18100 Armilla (Granada), Spain
[b] CIRIMAT, Université de Toulouse, CNRS, Ensiacet, 4 allée Emile Monso, 31030 Toulouse cedex 4, France
[c] Institute of Science and Technology for Ceramics (ISTEC), National Research Council (CNR), Via Granarolo 64, 48018 Faenza, (RA), Italy
[d] Dipartimento di Scienze della Salute, Università del Piemonte Orientale, Via Solaroli, 17, 28100 Novara, Italy
[e] Department of Analytical Chemistry, Faculty of Sciences, University of Granada, Avda. Fuentenueva s/n, 18071 Granada, Spain

GRAPHICAL ABSTRACT

Citrate functionalized calcium doped europium phosphate nanoparticles were crystallized by thermal decomplexing of Ca^{2+}/Eu^{3+}/citrate/phosphate/carbonate solutions. The crystallization mechanism, luminescence properties and cytocompatibility of this class of nanoparticles were investigated. These biocompatible nanoparticles appear as promising luminescent probes in the field of bioimaging.

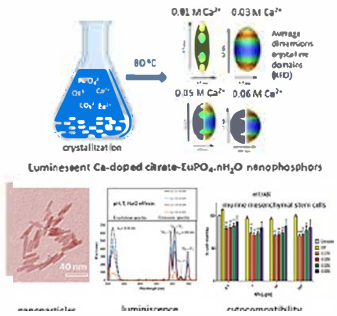

ARTICLE INFO

Keywords:
Ca-doped europium phosphates
Nanophosphors
Luminescence
Cytocompatibility

ABSTRACT

Biocompatible nanosystems exhibiting long lifetime (~millisecond) luminescence features are particularly relevant in the field of bioimaging. In this study, citrate functionalized calcium doped europium phosphates nanophosphors of the rhabdophane type were prepared at different synthesis times by a bioinspired crystallization route, consisting in thermal decomplexing of Ca^{2+}/Eu^{3+} /citrate/phosphate/carbonate solutions. The general formula of this material is $Ca_{\alpha}Eu_{1-\alpha}(PO_4)_{1-\alpha}(HPO_4)_{\alpha}\cdot nH_2O$, with α ranging from 0 to 0.58 and $n \sim 1$. A thorough characterization of the nanoparticles has been carried out by XRD (including data processing with Topas 6.0), HR TEM, TEM, FTIR, TG/DTA, ICP, dynamic light scattering (DLS), electrophoretic mobility, and fluorescence spectroscopy. Based on these results a crystallization mechanism involving the filling of cationic sites with Ca^{2+} ions associated to a concomitant adjustment of the PO_4/HPO_4 ratio was proposed. Upon calcium doping, the aspect ratio of the nanoparticles as well as of the crystalline domains decreased and the relative luminescence intensity (R.L.I.) could be

* Corresponding author.
E-mail address: jaime@lec.csic.es (J. Gómez-Morales).

https://doi.org/10.1016/j.jcis.2018.11.083

modulated. Neither the pH nor the ionic strength, nor the temperature (from 25 to 37 °C) affected signif icantly the R.L.I. of particles after resuspension in water, leading to rather steady luminescence features usable in a large domain of conditions. This new class of luminescent compounds has been proved to be fully cytocompatible relative to GTL 16 human carcinoma cells and showed an improved cytocompatibil ity as the Ca^{2+} content increased when contacted with the more sensitive m17. ASC murine mesenchymal stem cells. These biocompatible nanoparticles thus appear as promising new tailorable tools for biomed ical applications as luminescent nanoprobes.

1. Introduction

Materials at the nano scale possess unique optical, magnetic, and chemical properties which allow the creation of imaging probes with better contrast enhancement, increased sensitivity, improved signal to noise ratio and better spatial and temporal information in comparison to the conventional imaging agents [1]. Among them, luminescent nanoparticles are excellent optical probes that can significantly extend the capabilities of well established fluorophores such as organic dyes and genetically engi neered fluorescent proteins [2]. Their advantages include also excellent photostability, tunable and narrow spectra, controllable size, resilience to environmental conditions such as pH and temper ature, in combination with a large surface for anchoring targeting biomolecules [2]. Their function is mainly to provide the necessary fluorescent contrast required to visualize specific cellular compo nents and tissues [3]. Several luminescent nanomaterials including quantum dots [4], nanodiamonds [5], gold nanoparticles [6], nanos tructures labeled with organic dyes [7], nanocrystalline calcium orthophosphate apatites labeled with lanthanide ions or organic dyes [8 11] and others, have been proposed as fluorophores for these applications. In recent years, lanthanide orthophosphates ($LnPO_4$) have attracted much attention because they exhibit low solubility in water, high thermal conductivity and high refraction index, thus being candidates for a wide range of applications including phosphors, catalysts, sensors, heat resistant materials [12] and also, as optical probes for bioimaging [13,14]. As imaging agents the favorable features of lanthanide doped nanoparticles include large effective Stokes shift, sharp emission peaks with nar row band width, low photobleaching, stability to photochemical degradation, long luminescence lifetimes, low toxicity and the absence of blinking [10 15].

Lanthanide orthophosphates $LnPO_4\ nH_2O$ (n = 0 2) (Ln^{3+} = lan thanide ion) present five polymorphic modifications, i.e. monazite (monoclinic), xenotime (tetragonal), rhabdophane (hexagonal), weinschenkite (monoclinic) and orthorhombic [16]. The hexagonal structure is usually the low temperature phase and it can trans form into the monazite structure, while the tetragonal phase main tains its structure after calcination at 900 °C [17,18]. Different methods to prepare $LnPO_4\ nH_2O$ nanocrystals with controlled mor phologies such as nanorods, nanowires or nanocables have been proposed. Synthetic methods are based on high or low temperature approaches, such as hydrothermal synthesis [19 22], ultrasound irradiation [23], precipitation in oil baths [24], sol gel combined with electrospinning [25], surfactant assisted methods to mediate the slow crystallization of the nanocrystals [26], or else layer by layer deposition of precursors followed by crystallization at room temperature [27].

Among lanthanides ions, trivalent europium, Eu^{3+}, has been used to crystallize luminescent compounds such as $EuPO_4\ nH_2O$, or Eu^{3+} doped $LnPO_4$ of the hexagonal form with improved energy transfer efficiency between the $Ln^{3+}$and Eu^{3+} [14,27 29]. From another perspective, crystallization of $EuPO_4\ nH_2O$ has been also considered as a method to separate Eu^{3+} impurities from phospho ric acid solutions obtained from calcium phosphate apatite rocks [30,31]. The presence of Eu^{3+} impurities is assumed to result from Eu^{3+} to Ca^{2+} substitution in the apatite structure. Ca substituted $EuPO_4\ nH_2O$ crystallizes in such acid solutions due to the presence of Ca^{2+} as main impurity [31].

Luminescent Ln^{3+} doped calcium phosphate (apatite) nanopar ticles have been extensively studied as materials for diagnostics and therapeutic applications [10,11,13,14] while Ca substituted $EuPO_4\ nH_2O$ has never been proposed for similar topics. Compared to the precipitation of Ln^{3+} doped apatite nanoparticles [32,33], a main advantage of $EuPO_4\ nH_2O$ is related to its reduced polymor phism; the hexagonal rhabdophane structure being the crystalline phase that usually precipitates at low temperatures [28]. In con trast, during the calcium phosphate crystallization at low tempera ture several polymorphs, including monetite, brushite, octacalcium phosphate and apatite can eventually appear [34,35,36], depending on experimental conditions.

In the present work we have prepared Ca doped europium phosphate nanocrystals of the hexagonal phase employing a bioin spired synthetic route consisting in thermal decomplexing of Eu^{3+}/Ca^{2+}/citrate/phosphate/carbonate solutions method and assessed their luminescence and cytocompatibility properties. The pro posed technique, which was previously used to precipitate cal cium phosphate apatite nanoparticles doped with different metallic ions and coated with citrate [37 39], is one pot, straight forward, easily scalable to an industrial level, and respects the principles of green chemistry. The presence of Ca^{2+} in the structure of the nanocrystals as well as of citrate adsorbed on the surface of the constitutive particles (a feature found in bone apatite nanocrystals [40]) are expected to be beneficial from the point of view of the cytocompatibility that is required for bioimaging applications.

2. Materials and methods

2.1. Reagents

Europium chloride hexahydrate ($EuCl_3\ 6H_2O$, ACS Reagent, 99.9% pure), calcium chloride dihydrate ($CaCl_2\ 2H_2O$, Bioxtra, ≥ 99.0% pure), sodium citrate tribasic dihydrate ($Na_3(Cit)\ 2H_2O$ where cit = citrate = $C_6H_5O_7$, ACS reagent, ≥99,0% pure), sodium hydrogenphosphate (Na_2HPO_4, ACS reagent, ≥99.0% pure), sodium carbonate monohydrate ($Na_2CO_3\ H_2O$, ACS reagent, 99.5% pure), and hydrochloric acid (HCl, ACS reagent, 37 wt% in H_2O) were pro vided by Sigma Aldrich. All solutions were prepared with ultrapure water (0.22 μS, 25 °C, Milli Q, Millipore).

2.2. Precipitation method

Nanoparticles were synthesized as follows: a solution of com position (a) 0.12 M Na_2HPO_4, + 0.2 M Na_2CO_3, with pH adjusted to 8.5 with diluted HCl, was poured on a solution of composition (b) $x CaCl_2 + y EuCl_3$ + 0.4 M Na_3(cit) (with x) being the doping Ca^{2+} concentration 0.01, 0.03, 0.05 and 0.06 M and $y = 0.1\ \ x$ M) (1:1 v/v, 200 mL total) at 4 °C. The mixed solution was introduced

in a 200 mL bottle made of Pyrex® glass, sealed with a screw cap and, without delay, immersed in a water bath at 80 °C and then moved to an oven with circulated forced air at the same tempera ture. The experiments lasted between few minutes and few days. Once finished, the precipitates were subjected to 6 consecutive cycles of washing by centrifugation with ultrapure water to remove unreacted salts. Afterwards they were freeze dried over night at 50 °C under vacuum (3 mbar).

2.3. Characterization techniques

The precipitates were characterized by X ray powder diffraction (XRD), Fourier transform infrared (FTIR) spectroscopy, scanning and transmission electron microscopy (SEM, TEM), high resolution TEM (HR TEM), and fluorescence spectroscopy. Selected samples were analyzed by dynamic light scattering (DLS), ζ potential and thermo gravimetry/differential scanning calorimetry (TG/DTA). Ca, P and Eu contents were quantified by inductively coupled plasma optical emission spectrometry (ICP OES) spectrometer.

The X ray powder diffraction data were collected using a Bruker D8 Advance Vario diffractometer with a Bragg Brentano parafocus ing geometry and Cu $K_{\alpha 1}$ radiation (1.5406 Å). Data processing was conducted via the software TOPAS 6.0 [41]. The contribution of the anisotropic peak broadening due to domain size was modeled using the "AnisoCS" TOPAS macro developed by Ectors et al. [42,43] based on the size Voig approximation, and taking into account the instrumental contribution from a measurement of LaB6 standard (NIST SRM 660c). A biaxial ellipsoid model was selected to fit the experimental data, and the anisotropic sizes obtained are the main radii area weighted in nm.

Fourier transform infrared spectroscopy was used for comple mentary characterization of the samples. In a first stage, spectral acquisitions were run using a JASCO 6200 FTIR spectrometer equipped with an attenuated total reflectance (ATR) accessory. Subsequently, more in depth analyses were drawn from spectra recorded in transmission mode using a Perkin Elmer Spectrum One FTIR spectrometer using the KBr pellet method. The pellets were prepared by mixing ~1 mg of sample with ~100 mg of anhy drous KBr and then pressed with a hydraulic pump at 10 t into 7 mm diameter discs. Pure KBr pellets were used to record the background. FTIR spectra in transmittance mode were recorded within the wavelength range from 4000 cm^{-1} to 400 cm^{-1}.

TGA DTA analyses of the samples were carried out in a simulta neous thermal analyzer (STA 449 Jupiter Netzsch Geratebau, Selb, Germany). About 10 mg of sample was weighted in a platinum cru cible and heated from room temperature to 1000 °C under air flow with a heating rate of 10 °C/min.

The chemical composition of the samples was determined dis solving the samples in a diluted HNO_3 solution (~1 wt%) and then analyzed by an ICP OES (Liberty 200, Varian, US) employing wave lengths of 422.673 nm (Ca), 420.504 nm (Eu), and 213.618 nm (P).

Transmission electron microscopy (TEM) observations and selected area electron diffraction (SAED) analysis were performed with a TEM Libra 120 Plus instrument from Carl Zeiss microscope operating at 80 kV. Resolution point point is 0.34 nm and magnifi cation is 8 630,000x. Samples were dispersed in ethanol (absolute, ≥99.8%) using an ultrasound bath. Then a few droplets of the slurry were deposited on conventional copper microgrids with FORMVAR carbon film prior to observation. HR TEM analysis was performed with a TITAN G2 60 300 FEI Instrument operating at 300 kV. The instrument is equipped with EDX Super X detector to perform microanalysis and STEM type HAADF.

The analysis of the particle size distribution and electrophoretic mobility (transformed to ζ potential values) of suspensions was performed in a Zetasizer Nano ZS analyzer (Malvern, UK) using dis posable polystyrene cuvettes containing the particles suspended in deionized water (0.5 mg/mL) at 25 °C. Samples were immersed in ultrasonic bath for 5 min prior to DLS analysis. For the measure ments of the ζ potential versus pH the MPT 2 autotitrator (Mal vern, UK) connected to the analyzer was employed. Diluted HCl and NaOH solutions (0.25 and 0.1 M, respectively) were used as titration agents. No additional electrolytes were added.

2.4. Luminescence spectroscopy

Excitation and emission spectra of the solid samples as well as of aqueous suspensions of the nanoparticles (~0.5 mg/mL) were recorded using a Cary Eclipse Varian Fluorescence Spectropho tometer (Varian Australia, Mulgrave, Australia) with an R928 pho tomultiplier tube (Hamamatsu, Iwata gun, Shizuoka ken, Japan). For solid nanoparticles λ_{exc} was 394 nm, λ_{em} 614 nm, delay time (t_d) was 0.120 μs and gate time (t_g) was 5 ms. Spectra were recorded with a photomultiplier voltage of 500 V. The excitation and emission spectra were recorded within the range 250 500 nm and 500 750 nm respectively. For nanoparticles in aque ous suspensions, the following conditions were used: λ_{exc} 230 nm, λ_{em} 614 nm, t_d 0.120 μs and t_g 5 ms. In this case the pho tomultiplier voltage was 600 V and the excitation and emission spectra were recorded within the wavelength range 200 550 nm and 400 750 nm respectively.

2.5. Cytocompatibility tests

GTL 16 (a human gastric carcinoma cell line) and m17.ASC (a spontaneously immortalized mouse mesenchymal stem cell clone from subcutaneous adipose tissue) cells (12,000 and 5,000 cells/ well in 96 well plates, respectively) were incubated for 24 h and then different concentrations of the differentially doped (x = 0.01, 0.03, 0.05, 0.06 M Ca^{2+}) particles, ranging from 0.1 to 100 μg/ml, were added in 100 μL of fresh medium. After 72 h incubation, cell viability was evaluated by the 3 (4,5 Dimethylthiazol 2 yl) 2,5 di phenyltetrazolium bromide) (MTT, Sigma) colorimetric assay. Briefly, 20 μL of MTT solution (5 mg/ml in a PBS solution) were added to each well. The plate was then incubated at 37 °C for 3 h. After the removal of the solution, 125 μL of isopropanol, 0.2 M HCl was added to dissolve formazan crystals. 100 μL were then removed carefully and the optical density was measured in a multiwell reader (2030 Multilabel Reader Victor TM X4, PerkinEl mer) at 570 nm. Viability of parallel cultures of untreated cells was taken as 100% viability, and values obtained from cells undergoing the different treatments were referred to this value. Experiments were performed 4 times using 3 replicates for each sample.

Statistical Analysis. Data are expressed as mean ± standard devi ation of at least three replicates. Statistical analyses were per formed using a one way ANOVA with Bonferroni's post test for grouped analyses using GraphPad Prism version 4.03 for Windows, GraphPad Software (GraphPad Prism, San Diego, CA). Differences at $p < 0.05$ were considered to be statistically significant.

3. Results and discussion

3.1. Crystallographic, compositional, morphological and spectroscopic characteristics

The XRD patterns of samples precipitated in the presence of increased Ca^{2+} doping concentrations (x = from 0.01 to 0.06 M) at different maturation times are reported in Fig. 1.

The patterns mainly display the distinguishing reflections of the hexagonal phase of $EuPO_4$ nH_2O (rhabdophane), space group $P3_121$ (PDF 20 1044) with lattice constants a = 6.910 Å, and c = 6.340 Å.

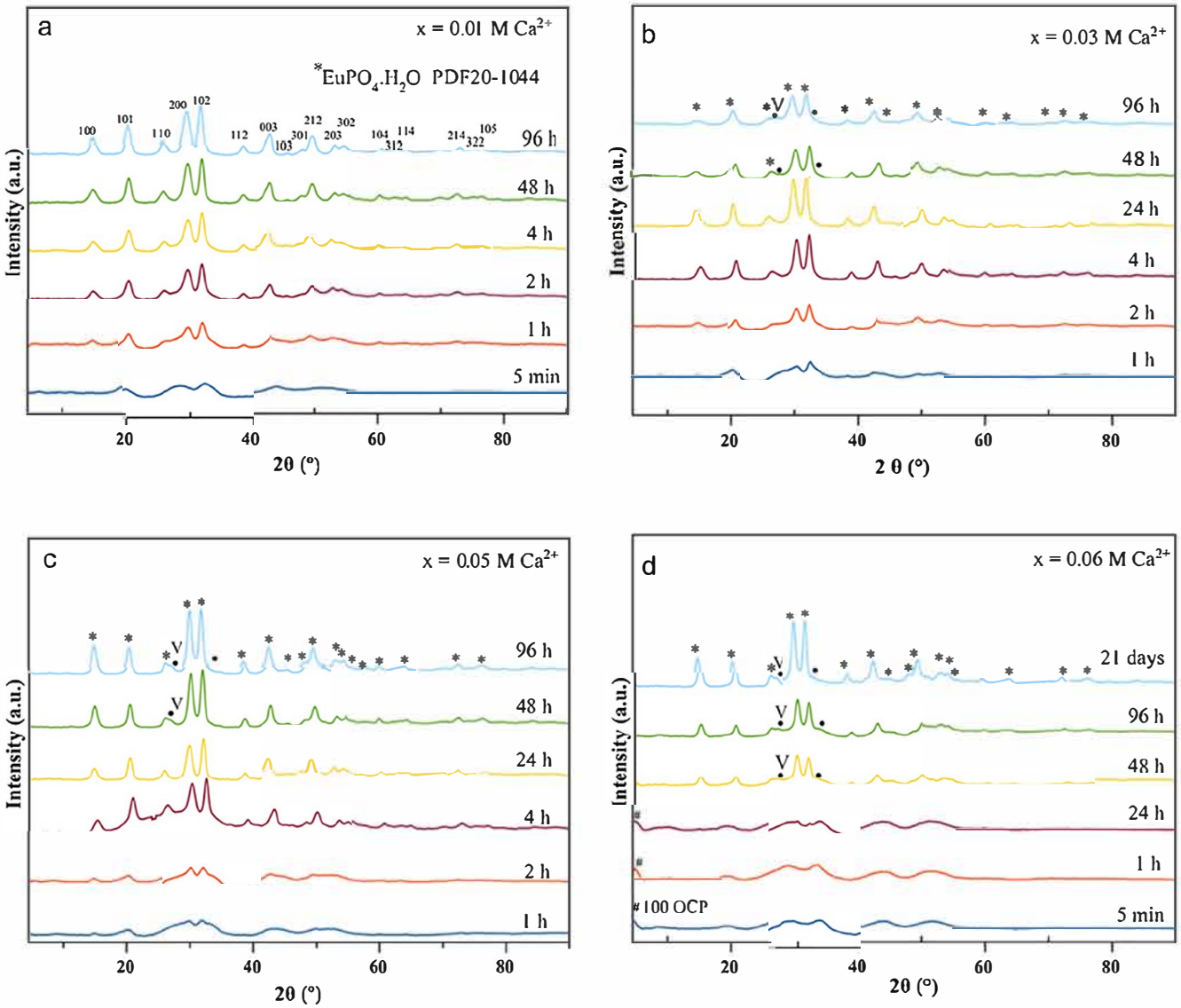

Fig. 1. X-ray diffraction patterns of the samples precipitated using increasing Ca^{2+} doping concentrations: (a) 0.01 M; (b) 0.03 M; (c) 0.05 M and (d) 0.06 M. *$EuPO_4{\cdot}H_2O$ (PDF 20-1044). # Reflection of (1 0 0) plane of octacalcium phosphate (OCP, PDF 44-0778). • Reflections (1 0 1) and (1 1 4) of $CaCO_3$ vaterite (V, PDF 33-0268).

The main reflections of this phase are situated at 2θ 14.67° (1 0 0), 20.35° (1 0 1), 25.80° (1 1 0), 29.77° (2 0 0), 31.95° (1 0 2), 38.44°(1 1 2) 42.61° (0 0 3) and 49.46° (2 1 2). The diffraction peaks at the shorter maturation times are broad and poorly defined sug gesting a relatively lower degree of crystallinity and nanodimen sions. The evolution with maturation time of the full width at half maximum (FWHM) of the two main reflections at 29.77° and 31.95° indicates an increase in size or crystallinity up to 48 h for x = 0.010 M Ca^{2+}, 24 h for x = 0.030 M Ca^{2+}, 96 h for x = 0.050 M Ca^{2+} and 21 days for x = 0.06 M Ca^{2+}. Only a small decrease in size or crystallinity can be deduced after 24 h matura tion for x = 0.03 M Ca^{2+}. No peaks assignable to other crystalline phase were identified when using the 0.01 M Ca^{2+} doping concen trations even for early precipitation times (Fig. 1a). On the con trary, the samples precipitated using the 0.06 M Ca^{2+} concentration show a different phase evolution (Fig. 1d). At matu ration times of 5 min, 1 h and 24 h the main reflection at 2θ = 4.74° assignable to (1 0 0) plane of octacalcium phosphate (OCP, PDF 44 0778) is present. The broad width of this reflection along with the bulging of the baseline in the 2θ range from 22° to 38° suggests the nanocrystalline character of the OCP phase. The peak at 4.74° was not observed in the samples matured for more than 24 h, which in tum, shows mainly the reflections of the hexagonal phase of $EuPO_4\,nH_2O$. Thus the formation of OCP in early stages was only transient until final ion reorganization of the system took place.

For Ca^{2+} doping concentrations x = 0.03, 0.05 and 0.06 M, traces of an additional phase start to appear at high maturation time, which is especially visible at around 2θ ~ 27.0 and 32.8°. These additional peaks detected for high calcium concentrations are attributed to the reflections (1 0 1) and (1 1 4) of $CaCO_3$ vaterite (PDF 33 0268), eventually doped with europium, which becomes stable in the calcium rich medium. According to ICP OES data (see below) an amount close to 0.4, 10 and 14 wt% respectively for 0.03, 0.05 and 0.06 M was evaluated for 96 h of maturation, besides the europium phosphate phase. In contrast, no vaterite was detected for the lowest Ca^{2+} concentration (x = 0.01 M) or for low maturation times, where the samples consist solely in single phased Ca doped $EuPO_4\,nH_2O$. Vaterite is a highly biocompatible allotropic form of calcium carbonate that is used in the biomateri als field, e.g. for the setup of bone cement formulations [44]. The eventuality of traces of this minor phase is thus not problematic *per se* for biomedical applications; in any case, we show here

the possibility to avoid its presence if needed, by adequately tailoring the precipitation conditions such as calcium doping concentration.

The microstructural study of samples matured for 96 h, analyzing the full XRD pattern of the Ca doped $EuPO_4\ nH_2O$ with TOPAS 6.0 software (Fig. 2 and Table 1), reveals a trend from elongated to more isometric shapes of the single crystal domains when increasing the Ca^{2+} doping concentration. The coherent length (L) of the domains (Table 1 and insets in Fig. 3) evolves from 13.3 ± 0.1 nm for the less Ca doped sample to 6.9 ± 0.2 nm for the highest Ca^{2+} concentrations. Similarly, the aspect ratio switches from 3.6 to 1.1. The sample obtained for × = 0.05 M Ca^{2+} displayed a coherent length and width almost doubled of that obtained for × = 0.03 M Ca^{2+} in spite of similar aspect ratios. Note that in all panels of Fig. 2, τ is slightly higher than 1.6, which indicates that the population of single crystal domains is polydisperse.

TEM observations (Fig. 3a d) allowed visualizing the morphology and average dimensions of the nanoparticles, which were found about 3 times larger than the sizes determined by Rietveld refinement. It is important to remark that TEM and XRD allow evaluating two different features of the material (observed particles size vs coherent size of crystal domains) therefore only the general trend of data can be compared.

The average dimensions of the particles determined by TEM (Table 1) typically varied from 40 ± 7 nm in length with the aspect ratio (length/width) of 5 for the less Ca doped sample (1.3 wt% Ca) to 19 ± 7 nm in length with the aspect ratio of 2.54 for the sample with the highest Ca content (14.2 wt% Ca). It is thus observed that increasing the Ca^{2+} content the nanoparticles are in general more isometric with ill defined shape. In the case of × = 0.05 M Ca^{2+} we found a mixture of elongated and ill defined isometric nanoparticles, therefore this doping point can represent the transition between these two morphologies.

Fig. 3e and f show the STEM images in bright field (BF) and high angle annular dark field (HAADF) of the less Ca doped sample. The indexed SAED pattern (Inset of Fig. 3f) of this sample shows the crystallographic planes of the hexagonal rhabdophane phase, i.e. (1 0 1), (1 1 0), (2 0 0), (1 0 2), (1 1 2), (2 1 2), (3 0 0) and (3 2 2). HRTEM images of the same sample (Fig. 3g and h) reveal the lattice fringes of the nanoparticles, mostly structured as single crystal domains, whose d spacings correspond to planes (2 0 0) and (1 0 2) as also revealed in the FFT images (insets of Fig. 3g and h). The elemental mappings of the less Ca doped nanoparticles (Fig. 3i l) show a homogeneous distribution of Ca, Eu, O and P.

TGA DTA analyses (see SI, Fig. S1) revealed a rather comparable behavior for all samples, and the data are very close to those

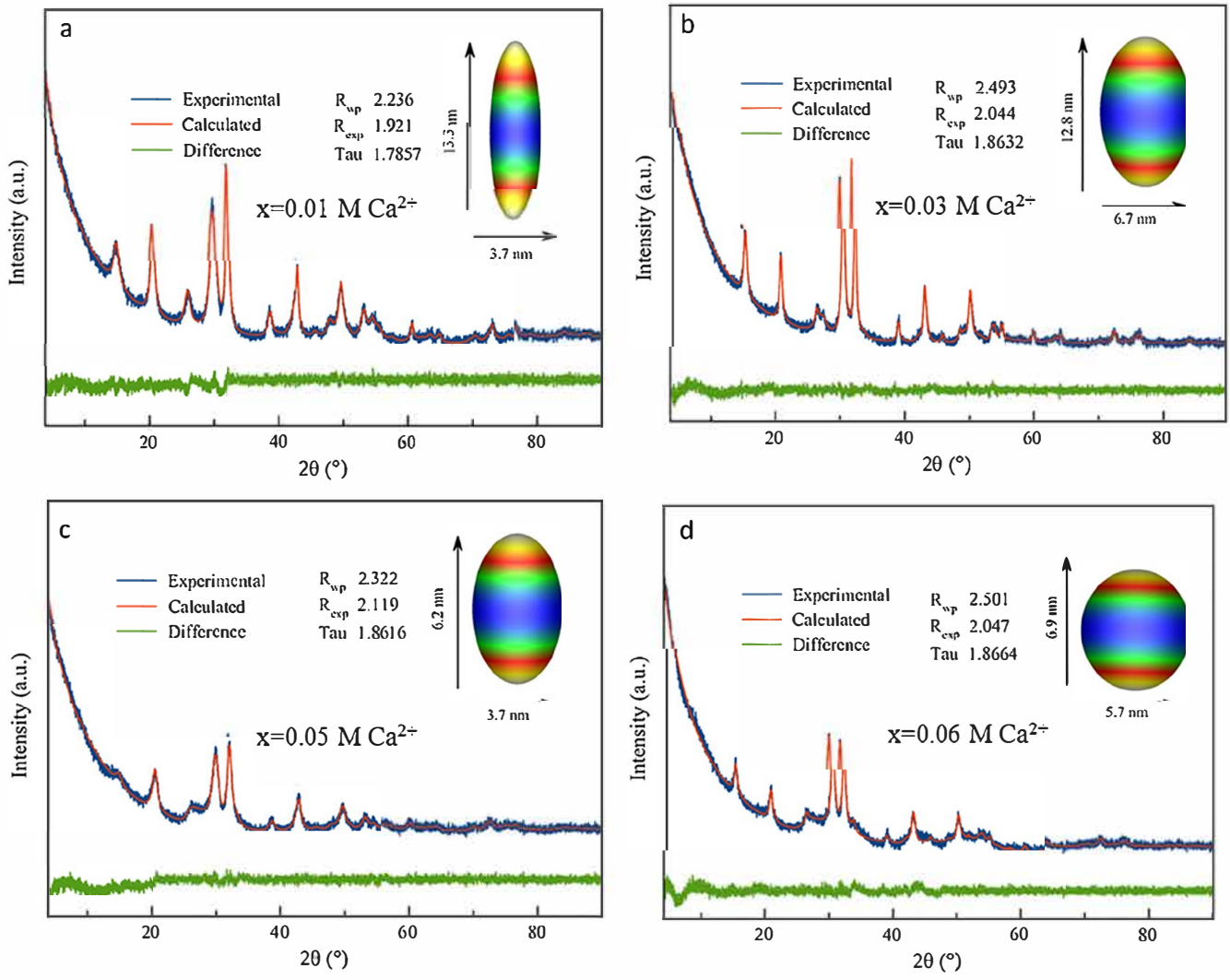

Fig. 2. Microstructural evolution of the single crystal domains of Ca-doped $EuPO_4{\cdot}nH_2O$ nanoparticles of samples precipitated at 96 h using the Ca^{2+} doping concentrations: (a) 0.01 M; (b) 0.03 M; (c) 0.05 M and (d) 0.06 M. The two XRD vaterite reflections are excluded. R_{wp} and R_{exp} are agreement factors in % for the refinement. τ is a polydispersity factor ($1 \leq \tau \leq 2$), being 2 the theoretical limit for the Gaussian part of the size Voig approximation used.

reported for similar materials [45 48]. The main weight losses occurred in the range T_{room} 700 °C corresponding to the loss of adsorbed and structural water, while the weight loss between 700 and 1000 °C, that is more evident in the samples prepared using the higher Ca^{2+} doping concentrations, is associated to the loss of CO_2 from the carbonate decomposition of vaterite. In details, the first weight loss of about 2 6 wt%, attributed to the residual adsorbed water on the powder surface due to the storage

Table 1
Quantitative compositional, elemental chemical analysis and average size (length and width) of Ca-doped cit-$EuPO_4{\cdot}nH_2O$ samples prepared with Ca^{2+} doping concentration *x* from 0 to 0.06 M, at 96 h.

Ca^{2+} mol/L	Value[g] of α (±0.05)	Analyzed Elements (wt.%)					Calculated oxide components (wt.%)[e]			Total[f] (wt.%)
		Eu[a]	Ca[a]	P[a]	H_2O Adsorbed[b]	H_2O Structural[b]	Eu_2O_3	CaO	P_2O_5	
0	0	53.0 ± 3.0	0	10.6 ± 0.6	6.0 ± 0.6	5.8 ± 0.7	61.4 ± 1.2	0	24.3 ± 1.0	100.2 ± 3.1
0.01	0.09	51.0 ± 2.0	1.3 ± 0.1	11.9 ± 0.4	2.1 ± 0.2	5.4 ± 0.5	61.7 ± 1.2	1.9 ± 0.1	28.5 ± 1.0	100.0 ± 3.1
0.03	0.30	43.7 ± 0.3	4.9 ± 0.1	12.6 ± 0.1	3.7 ± 0.4	6.2 ± 0.6	52.4 ± 0.3	7.1 ± 0.1	29.9 ± 0.2	100.3 ± 1.7
0.05	0.49	31.5 ± 0.1	11.6 ± 0.1	12.6 ± 0.1	4.3 ± 0.4	6.6 ± 0.7	37.5 ± 0.1	16.7 ± 0.1	29.6 ± 0.2	100.5 ± 1.7
0.06	0.58	26.2 ± 0.3	14.2 ± 0.1	12.6 ± 0.2	5.6 ± 0.6	6.4 ± 0.6	30.8 ± 0.3	20.2 ± 0.2	29.3 ± 0.4	100.1 ± 2.3
		Rietveld Refinement[c] (TOPAS 6.0)					TEM[d]			
		Length (L, nm) Width (W, nm)			R_1 (L/W) aspect ratio		L, nm W, nm		R_2 (L/W) aspect ratio	
0.01		13.3 ± 0.1 3.7 ± 0.3			3.6		39.5 ± 7.1 7.9 ± 1.6		5.0	
0.03		6.2 ± 0.2 3.7 ± 0.3			1.7		19.7 ± 3.2 6.9 ± 2.6		2.8	
0.05		12.8 ± 0.1 6.7 ± 0.2			1.9		41.1 ± 7.1 16.4 ± 5.7		2.5	
0.06		6.9 ± 0.2 5.7 ± 0.2			1.1		19.3 ± 6.9 7.6 ± 2.0		2.5	

[a] Measured by ICP-OES;
[b] measured by TGA-DTA.
[c] average dimensions (coherent length and width) of the single crystal domains determined by Rietveld refinement of the full diffraction pattern with TOPAS 6.0;
[d] average dimensions of the nanoparticles determined by TEM;
[e] without mentioning here H_2O, citrate and carbonate ions;
[f] counting H_2O, citrate and carbonate (vaterite) ions;
[g] value of α in the chemical formula $Eu_{1-\alpha}Ca_{\alpha}(PO_4)_{1-\alpha}(HPO_4)_{\alpha}{\cdot}nH_2O$

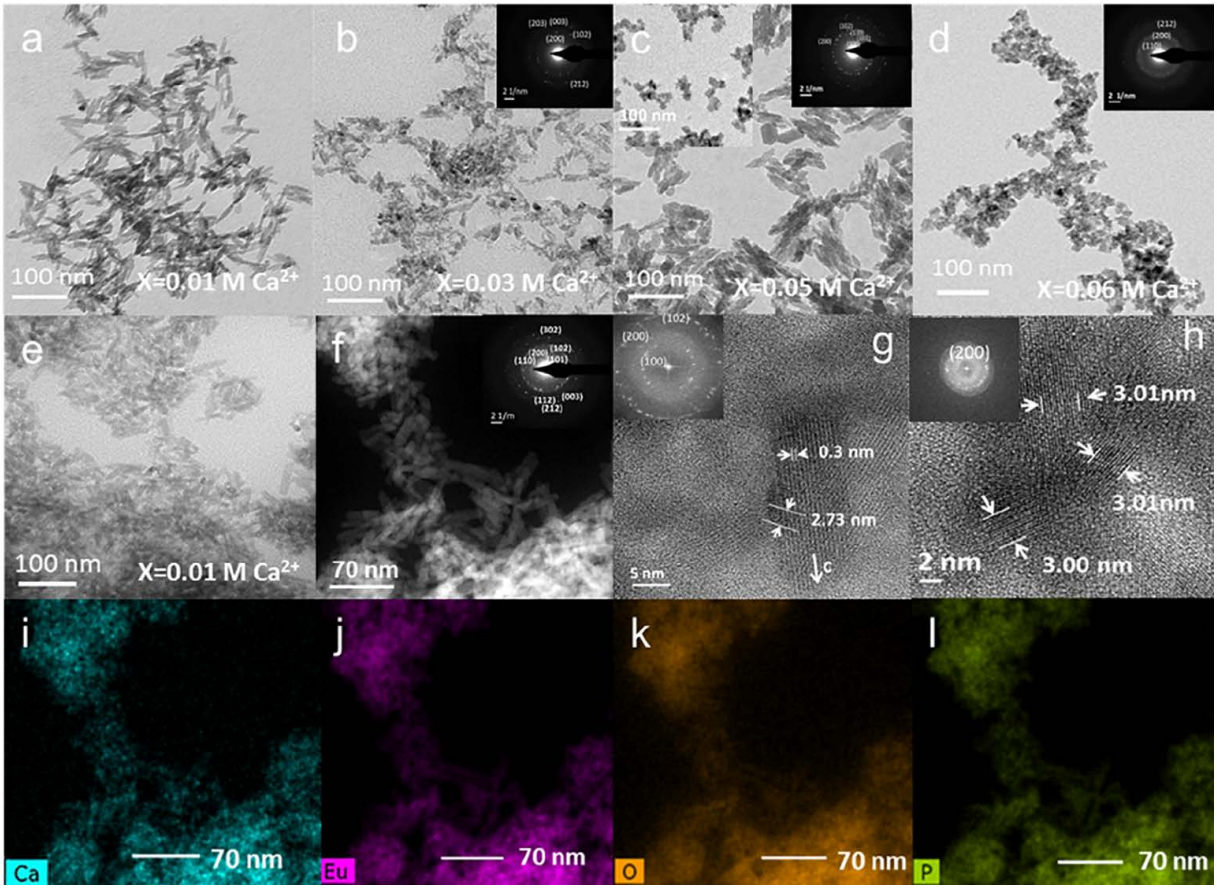

Fig. 3. (a–d) TEM micrographs of Ca-doped cit-$EuPO_4{\cdot}H_2O$ nanoparticles prepared with different Ca^{2+} doping concentrations at 96 h: (a) 0.01 M; (b) 0.03 M; (c) 0.05 M and (d) 0.06 M. Insets show the indexed SAED patterns of the nanoparticles. (e, f) BF HAADF-STEM micrographs of the sample prepared with the Ca^{2+} doping concentration of 0.01 M Ca^{2+} Inset in (f) shows the indexed SAED pattern. (g,h) HR-TEM images showing some lattice fringes and d-spacing of the sample prepared with the Ca^{2+} doping concentration of 0.01 M. Insets show the corresponding FFT images displaying the (1 0 0), (2 0 0) and (1 0 2) planes. (i–l) EDX Element mapping analysis of the sample displayed in panel f.

conditions in air, was found up to 120 °C with a broad endothermic peak in the range 50 100 °C in the DTA curve. The second weight loss began at about 120 °C and finished at about 700 °C. It corresponds to the dehydration (release of structural water) of the hexagonal phase. This step proceeded in two sequences. An important weight loss was registered up to about 350 °C and then it decreased slowly to 700 °C. This event was accompanied by a broad endothermic effect. The exothermic peak in the range 750 950 °C represents the phase transformation of the lanthanide orthophosphate from hexagonal to monoclinic [28].

Table 1 gathers the compositional information relative to the samples. In particular two interesting findings can be pointed out: (i) while the P wt% remained almost constant in all samples, the Ca wt% increased and the content of Eu accordingly decreased; (ii) the weight loss corresponding to the structural H_2O accounts for about 5 7 wt%, which is equivalent to a hydration content n of about 1 mol of H_2O (Table 1).

On the basis of these analyses, it is interesting to examine in further details the chemical composition of the samples. Phosphate groups are large ionic entities ensuring, as in many phosphate compounds such as apatites, the stability of the crystallographic structure. Therefore, the existence of phosphate vacancies is very improbable as this would most likely destabilize the whole structure. Also, the carbonation of $LnPO_4$ phases has not been reported to our knowledge. Yet, since the crystal electroneutrality has to be preserved upon Ca for Eu substitution, the replacement of trivalent Eu^{3+} cations by divalent Ca^{2+} should be undergone with simultaneous protonation of an equivalent number of PO_4^{3-} ions into HPO_4^{2-}. This presence of HPO_4^{2-} ions in calcium doped europium phosphate has already been considered in the literature.[31] This leads for the samples generated in the present study, and excluding citrate for simplicity of writing, to the general formula $Eu_{1-\alpha}Ca_\alpha(PO_4)_{1-\alpha}(HPO_4)_\alpha\, nH_2O$ with $0 \leq \alpha \leq 1$. From ICP data, the estimated value of "α" ranges between 0 and 0.58 for $\times$ varying from 0 to 0.06 M Ca^{2+}. For samples corresponding to $\times$ = 0.03, 0.05 and 0.06 M, an additional amount of vaterite is then also present, reaching 0.01, 0.22 and 0.30 mol per mole of europium phosphate, respectively.

For complementary characterization of the samples, FTIR spectroscopy was also applied, and Fig. 4a d show the spectra of the samples obtained upon increasing Ca^{2+} doping concentration. They display similar spectroscopic features and show the expected global shape of a rhabdophane phase [45,48] with a broad band in the range 1000 1100 cm^{-1}, related to the asymmetric stretching mode of PO_4^{3-} groups (υ_3 PO_4), and two intense bands at ~620 and 535 cm^{-1} due to the bending mode of PO_4^{3-} ions (υ_4 PO_4). The broad band observed between 3600 cm^{-1} and 2600 cm^{-1} corresponds to the O—H stretching from the associated water. Several spectral contributions also point to the presence of citrate molecular ions, with contributions at 2926 and 2856 cm^{-1} assignable to the

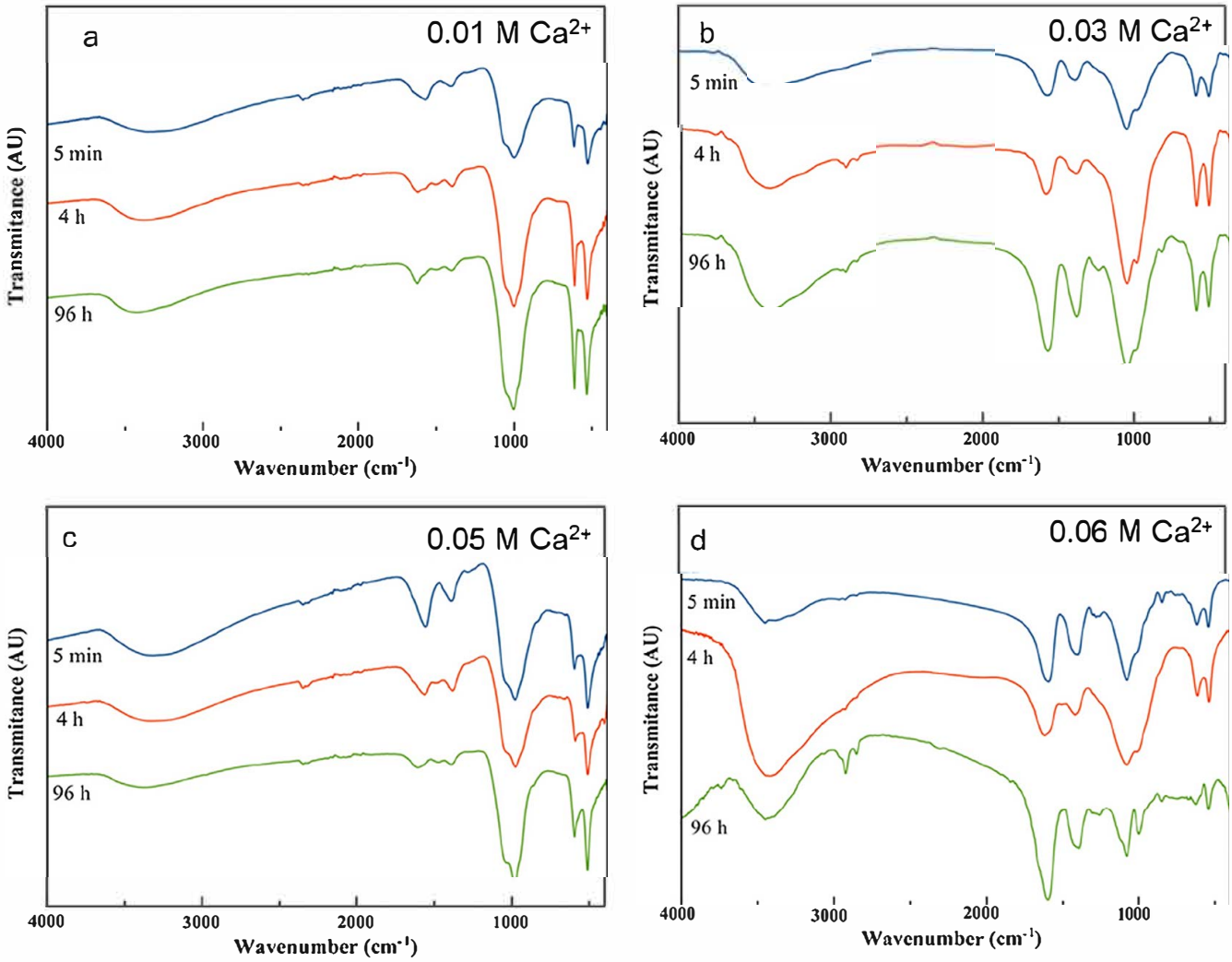

Fig. 4. (a–d) FTIR spectra of samples synthesized at Ca^{2+} doping concentrations 0.01, 0.03, 0.05 and 0.06 M at different maturation times.

stretching vibration of CH_2 groups [49], a small band detected here around 867 cm ^{1} which can be related to the bending mode of COO— groups [50], and broad signals at about 1590 cm ^{1} and 1402 cm ^{1} assignable to the antisymmetric and symmetric stretching of carboxylate (—COO) groups of the adsorbed citrate, respectively [51].

Traces of $CaCO_3$ vaterite have been revealed previously from XRD analysis for x = 0.003, 0.05 and 0.06 M Ca^{2+}, at least at high maturation times. The presence of this secondary phase explains the modifications observed in the 830 890 cm ^{1} and 1250 1550 cm ^{1} ranges (e.g. for 96 h of maturation, see ES, Fig.S2). In these regions are located not only COO vibrations from citrates, as mentioned above, but also of carbonate ions when present (respectively their ν_2CO_3 and ν_3CO_3 vibration modes). The contri butions initially present at 867 and 1402 cm ^{1} for low Ca doping and single phased systems are shifted to around 872 and 1412 cm ^{1} in the case of samples x = 0.05 and 0.06 M Ca^{2+}, which can be explained by the co presence of traces of vaterite [52] known to lead to vibration bands at 870 and 1420 cm ^{1}. It may also be noted that the presence of HPO_4^{2} ions, which is expected to give a band around 870 880 cm ^{1}, cannot be detected in this work due to the presence of other vibration due to citrates and car bonates in the same domain.

3.2. Crystal size distribution and electrokinetic properties (ζ potential) by DLS

The analysis of crystal size distribution (CSD) and surface ζ potential is fundamental to evaluate the potential applications of nanoparticles as drug delivery vehicles or as luminescent probes in medical imaging [53]. In the present study it was decided to plot the volume based frequency distribution of the different Ca^{2+} doped cit $EuPO_4$ H_2O samples because they clearly show the per centiles of the distribution D_{10} and D_{50} (Fig. 5a and S3 of SI). These percentiles represent the percentage of cumulative volume under size distribution (percentage of the population smaller than the size indicated). Thus, D_{10}, which is the percentile more close to the size of the fine individual particles, is always within the nanometer size range while D_{50}, which represent the median diameter of the CSD, is here partially influenced by particle aggre gation. D_{90} (not shown) is fully influenced by the aggregation of nanocrystals.

It is worth mentioning that median diameters for samples pre pared with x = 0.01 (D_{50} = 44 nm), 0.05 (D_{50} = 164 nm) and 0.06 M Ca^{2+} (D_{50} = 80 nm) are quite close to those of D_{10} (28, 38 and 52 nm, respectively) and that D_{10} defines well the size of individual nanoparticles, particularly for x = 0.01 and 0.05 M Ca^{2+} (L mea sured by TEM of 39.5 and 41.1 nm, respectively). This fact indicates that aggregation is very low below the median diameter of the CSD and negligible below D_{10}. Considering that ζ potential of the sus pension affects the aggregation state of the nanoparticles, i.e. the lower the absolute value of the ζ potential the greater the trend to aggregation, it is deduced that the interactions among nanopar ticles are very weak. The aggregates are broken only after 5 min sonication, in spite of the low values of the ζ potential at any of the pHs analyzed (Fig. 5b). Only for x = 0.03 M Ca^{2+}, with D_{50} 955 nm and D_{10} 68 nm the aggregation process is more important. For this sample the ζ potential within the pH range from 4 to 10 is closer to zero. We have not found a general trend relating the evo lution of the CSD with the Ca^{2+} doping concentration nor with the maturation time of the precipitates (see Fig. S3a d).

The above findings confirm that we succeeded in preparing Ca doped cit$EuPO_4$ nH_2O nanoparticles of the hexagonal rhabdophane phase with a tailored Ca^{2+} content and adsorbed citrate on their surface, a chemical feature which is also exhibited by bone apatites [40]. The aspect ratio of both the single crystal domains and the observed nanoparticles decreased as the Ca^{2+} content increases. To explain these results an important issue is the analysis of the growth behavior of the lanthanide orthophosphates. In general, those crystals with hexagonal rhabdophane type structure grow along the [0 0 1] direction resulting in the formation of nanowires or nanorods. The growth morphology, however, results from the interplay between the growth rates of the outermost crystallo graphic planes of the nanocrystals and the inhibiting/promoting effect of the additives or templates in solution. Therefore, the first key influence to consider when analyzing the morphology is that of the crystalline structure.

The overall rhabdophane structure has been described as col umns built up of alternate lanthanide ions, with eight fold coordi nation, and tetrahedral orthophosphate ions [12]. These columns, or periodic bond chains, are extended along the *c* axis, each one linked to four neighboring columns, consequently forming open channels that run through the structure along the c axis. These large channels incorporate structural H_2O molecules, between 0.5 and 2 molecules per formula unit, which might stabilize the hexag onal crystal structure [28,54]. From a thermodynamic point of view the activation energy for crystal growth along the c axis must be lower than that in perpendicular directions along the *a* or

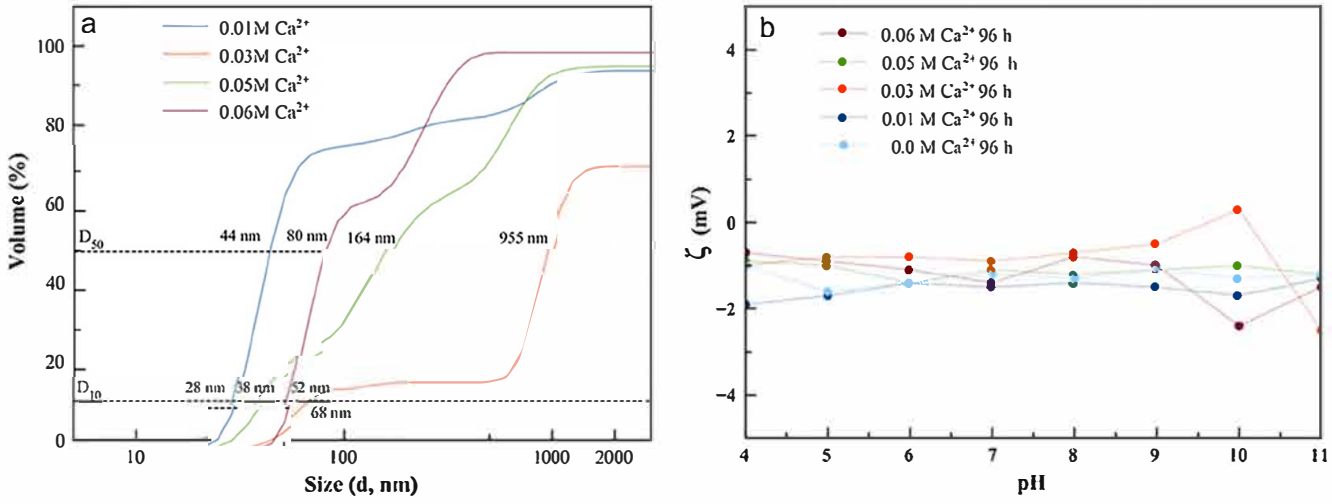

Fig. 5. (a) Cumulative volume oversize distribution of the Ca-doped cit-$EuPO_4$·nH_2O nanocrystals prepared at 96 h. (b) ζ-potential vs pH of cit-$EuPO_4$·nH_2O and Ca-doped cit-$EuPO_4$·nH_2O nanocrystals prepared at 96 h.

b axis, thus indicating that [0 0 1] will be the preferential growth direction.

A second key influential factor is linked to the presence of additives in the solution. Citrate ions are expected to play here two different roles during the precipitation of the nanoparticles: (i) it is a medium strength $M^{2+/3+}$ ligand that enables the preparation of metastable Ca^{2+}/Eu^{3+}/citrate/phosphate/carbonate solutions at slightly basic pH; these complexes can be easily destabilized by increasing the temperature, thus releasing the $M^{2+/3+}$ ions and leading to the precipitation of the Ca^{2+} doped nanoparticles. (ii) After the nucleation event the embryonic nanoparticles, initially amorphous, quickly transformed to crystalline nanophases, which may also be influenced by citrate ions. Taking into account their 3 peripheral carboxylic acid heads, free citrate ions may selectively adsorb on specific outermost planes of forming nanophases, slowing down in particular the growth along the [0 0 1] direction, thus leading to the formation of nanorods instead of long nanowires with high aspect ratios. Most probably these planes are {*h* 0 0} and {h 0 l} since faces (1 0 0) and (1 0 1) are displayed on the growth morphology (Fig. 3g).

The trend to lower aspect ratios and formation of ill defined morphologies in the nanoparticles described in this work is thus attributed not only to the effect of incorporating Ca^{2+} in their crystal structure, which affects the type of periodic bond chains, but also to the above effect of citrate. The formation of nanoparticles with lower aspect ratios was also found in other doped nanoparticles in carboxylate free solutions, i.e. doped apatite [55], thus probing that metal ions also contribute to the inhibiting effect of crystal growth along the [0 0 1] direction.

It is also worth noting the behavior of the nanoparticles in water suspensions. We have found that in some of the samples the trend to aggregate is low below the median diameter of the CSD and negligible below D_{10}.

In all samples the ζ potential values are slightly negative at pH 7 and 5 (Fig. 5b). These pH values are close to the physiological pH in blood circulation and to the more acidic pH in the endosome lysosome intracellular compartment, respectively. These low negative values of the ζ potential can be explained on the basis of the balance between the interactions of the negatively charged free carboxylate groups (—COO) of the adsorbed citrate molecules with the aqueous medium and those with the solid phase. The former should be weaker than the latter, i.e. electrostatic interaction of the —COO groups with the partially charged surface groups > $Eu^{\delta+}$ > $Ca^{\delta+}$, > $PO_4^{\delta-}$ of the outermost layer of the nanoparticle surfaces, thus exposing less ionic charge toward the medium. This detail indicates that interactions between nanocrystals within the nanosized range are very weak, so that dispersion is easily achieved by simple agitation, sonication, or else, by a subsequent functionalization of the nanoparticles with a biocompatible ligand.

3.3. Luminescence properties of Ca doped cit $EuPO_4$ nH_2O nanoparticles

3.3.1. Luminescence in solid state

It is well known that some lanthanides, especially europium (III) and terbium (III), form highly fluorescent chelates with many different organic ligands [56]. The sensitized fluorescence results from the ligand absorbing light, the energy of which is then transferred to the chelated metal ion. In fact, Eu(III) emits the energy as narrow banded, line type fluorescence with a long Stokes shift (over 250 nm) and an exceptionally long fluorescence decay time (up to 1 ms) [56]. Because of the long fluorescence decay time (over 10 times longer than the average background fluorescence) of Eu(III), a delay time (t_d) and a gate time (t_g) can be used during the measuring, remarkably reducing the background fluorescence.

The luminescence properties of solid Ca doped cit $EuPO_4$ nH_2O samples are practically the same as those depicted in Fig. 6 which correspond to × = 0.03 M Ca^{2+}; neither the maturation time nor the Ca^{2+} doping concentrations affect the excitation and emission wavelengths.

The observed excitation wavelengths for the powder were 319, 362, 379, 394 and 465 nm which correspond to the Eu^{3+} ion $^7F_0 \rightarrow {}^5H_6$, $^7F_0 \rightarrow {}^5D_4$, $^7F_0 \rightarrow {}^5L_7$, $^7F_0 \rightarrow {}^5L_6$, and $^7F_0 \rightarrow {}^5D_2$ transitions, and the emission wavelengths were 577, 590, 614, 650 and 699 nm, which correspond to the Eu^{3+} ion $^5D_0 \rightarrow {}^7F_0$, $^5D_0 \rightarrow {}^7F_1$, $^5D_0 \rightarrow {}^7F_2$, $^5D0 \rightarrow {}^7F_3$ and $^5D_0 \rightarrow {}^7F_4$ transitions, respectively [57]. This was expected because the electronic transitions of f orbitals are not affected by crystal's field.

The emission wavelength corresponding to the hypersensitive transition ($^5D_0 \rightarrow {}^7F_2$, 614 nm) produces the highest relative luminescence intensity. This is in agreement with the literature because this emission dominates the spectrum for nanosized particles [28]. Therefore, the optimum excitation and emission wavelengths of solid Ca doped cit $EuPO_4$ nH_2O were 394 nm and 614 nm, respectively.

Figure S4 (see SI) shows the effects of Eu (wt%), adsorbed water (wt%) and adsorbed citrate (wt%) from Table 1 on the relative luminescence intensity (R.L.I). We deduce that the R.L.I. determined in solid state is not affected by only one of these parameters individually. We can see, for instance, that the variation of R.L.I. with adsorbed water is abnormal, because water is a well known quencher of the luminescence. In the same way, we cannot establish a linear relationship between R.L.I. and adsorbed citrate. Most likely several phenomena must overlap and compete (quenching, auto bleaching, energy transfer, effect of chemical structure and so on) that make complex the interpretation of the luminescent behavior in solid state. Anyway, as the main objective of these materials is to be employed for imaging applications, therefore dispersed in aqueous media, a deeper discussion of these aspects affecting the luminescence in solid state are out of the scope of this piece of work.

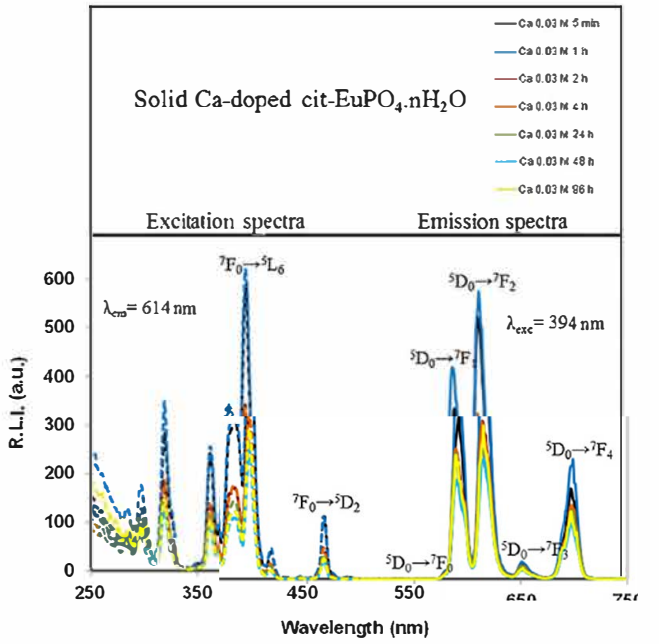

Fig. 6. Excitation (dashed lines) and emission (solid lines) uncorrected spectra of Ca-doped cit-$EuPO_4$·nH_2O prepared with × = 0.03 M Ca^{2+} at maturation times of 5 min, 1 h, 2 h, 4 h, 24 h, 48 h and 96 h. Slit-widths$_{exc/em}$ = 5/5 nm, t_d = 120 μs and t_g = 5 ms.

An important parameter in luminescent complexes is the luminescence lifetime (τ). The decrease of the R.L.I. versus time for pure cit $EuPO_4$ nH_2O (x = 0 M Ca) and for samples prepared with doping concentrations x = 0.01, 0.03, 0.05 and 0.06 M at 96 h is shown in Fig. S5 of SI. For each case, the decay profile was analyzed as a single exponential component ($R.L.I. = A\ e^{-t/\tau} + C$) obtaining τ of 904, 1029, 1119, 1294 and 1083 μs, respectively. It is possible to deduce that the luminescence lifetime for all materials is almost the same, of the order of the millisecond. This order of magnitude is similar to that of colloidal apatite nanoparticles stabilized with a phospholipid moiety, AEP [58], and points out a long luminescence lifetime as compared to the auto fluorescence of biological matter (of the order of the nanosecond), thus allowing us to envision applications as biomedical probes.

3.3.2. Luminescence in aqueous suspension

The luminescence properties of Ca doped cit $EuPO_4$ H_2O samples suspended in water are depicted in Fig. 7, which shows the uncorrected excitation and emission spectra. The maximum excitation wavelength observed was 230 nm. This transition corresponds to an electron that is transferred from the oxygen 2p orbital to an empty 4f orbital of the Europium, which is ascribed as a charge transfer state band [59–61].

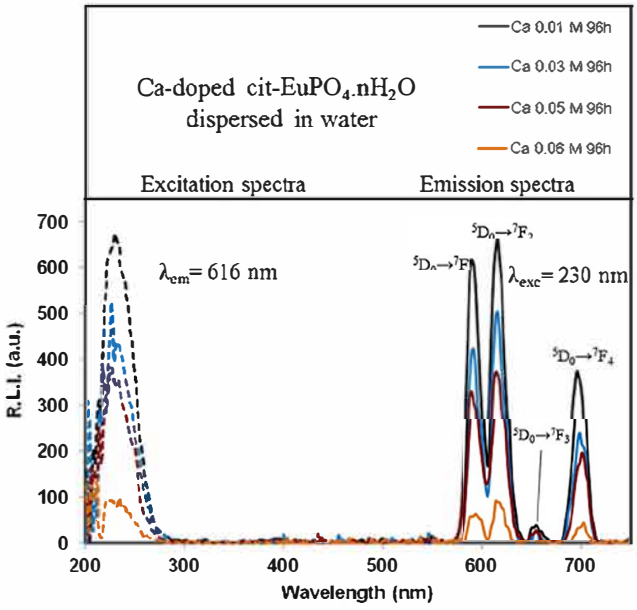

Fig. 7. Excitation (dashed line) and emission (solid line) spectra of Ca-doped cit-$EuPO_4{\cdot}nH_2O$ samples prepared with different Ca^{2+} doping concentrations at 96 h suspended in water at 25 °C and pH = 7.0. Slit-widths$_{exc/em}$ = 5/5 nm, t_d = 120 μs and t_g = 5 ms.

The observed emission wavelengths were 590, 616, 647 and 696 nm, which correspond to the Eu^{3+} ion $^5D_0 \rightarrow {}^7F_1$, $^5D_0 \rightarrow {}^7F_2$, $^5D_0 \rightarrow {}^7F_3$ and $^5D_0 \rightarrow {}^7F_4$ transitions, respectively [57]. The emission wavelength corresponding to the hypersensitive transition ($^5D_0 \rightarrow {}^7F_2$, 616 nm) produces the highest relative luminescence intensity, which once again agrees with the nanosized character of the material [28]. Therefore, the optimum excitation and emission wavelengths of the Ca doped cit $EuPO_4$ nH_2O materials dispersed in water were 230 nm and 616 nm, respectively.

On the other hand, it is also possible to observe that an increase on the Ca^{2+} doping concentration (which is related with a decrease of Eu^{3+} content in the material) decreases the luminescence of the materials suspended in water. Analyzing the variation of the luminescence versus the Eu wt% according to Table 1, it is possible to establish a positive linear relationship (see Fig. 8a). Then, in this case, the luminescence variations are basically attributed to the amount of Eu in the materials and, therefore, all the effects that perturb the luminescence on solid state must be attenuated in the aqueous medium.

It is well known that the media affect the luminescence intensities of luminophores [62]. To obtain a deeper understanding, the effects of pH, ionic strength and temperature were evaluated.

The influence of pH on the luminescence intensity was studied over the range 5.0 7.4 (Fig. 8b) and the effect of ionic strength was evaluated by suspending the particles in 0, 25, 50, 75 and 100 mM NaCl solutions (see SI, Fig. S6). It is possible to deduce that neither the pH nor the ionic strength affect significantly the R.L.I. of the suspended materials, which is important for the final applications of these nanoparticles.

The temperature may also theoretically affect the luminescence by quenching of the excited states; i.e. increasing T increases the molecular motion and collisions, and hence decreases the luminescence emission by increasing encounters probabilities [63]. Fig. S7 of SI shows the experimental results. To sum up, increasing from 25 to 37 °C does not affect the luminescence emission of all the tested materials in aqueous suspension (0.05 and 0.01 M Ca^{2+}, maturation time of 96 h). The change in fluorescence intensity is normally 1% per degree Celsius [63] and the decreases for these materials were 0.6 and 1.0% per degree Celsius, respectively. This is very important in view of medical and biomedical imaging (~ 37.4 °C).

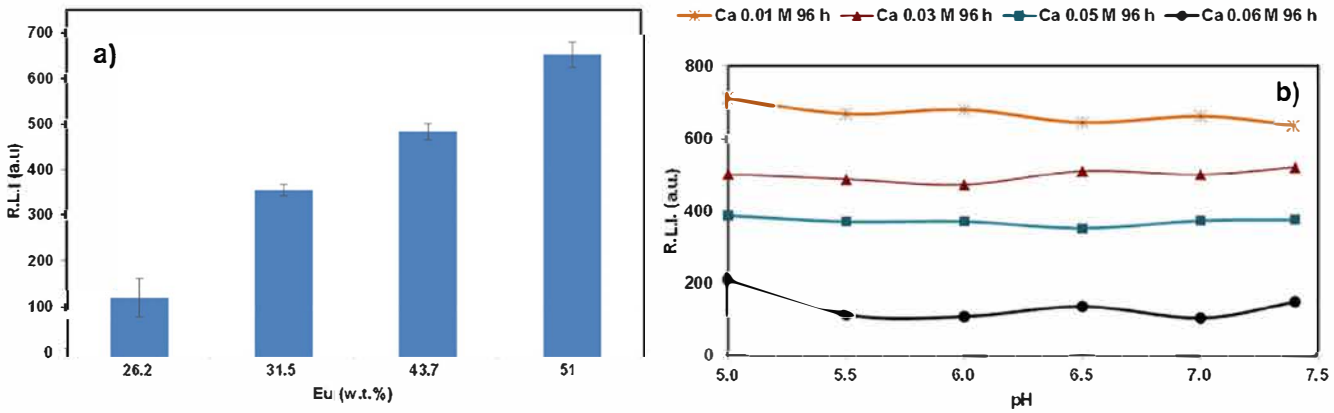

Fig. 8. Variation of R.L.I. of Ca-doped cit-$EuPO_4{\cdot}nH_2O$ samples dispersed in aqueous solution at 25 °C: (a) with wt % Eu at pH = 7 and (b) with the pH. $\lambda_{exc/em}$ = 230/614 nm, slit-widths$_{exc/em}$ = 5/5 nm, t_d = 120 μs and t_g = 5 ms.

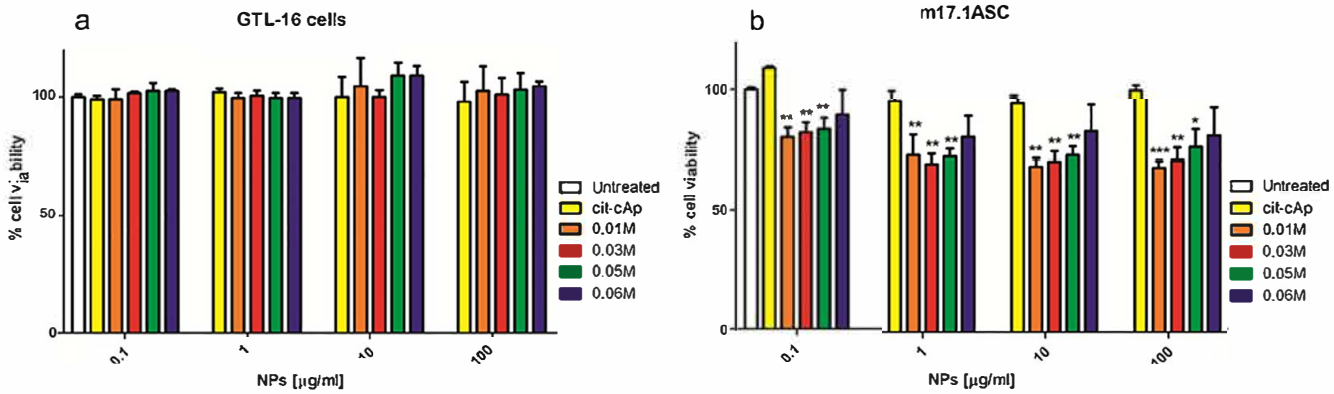

Fig. 9. Viability of GTL-16 cells (a) and of m17.ASC cells (b) incubated with Ca-doped cit-$EuPO_4{\cdot}H_2O$ particles doped with different concentration of Ca^{2+} for three days. Viability was assessed in MTT assays. Data represent means ± sd of three independent experiments performed in quadruplicate and statistical analyses were carried on using One-way ANOVA, with Bonferroni comparison test. For statistical analysis all data were compared to untreated samples ($^{*}p \leq 0.05$, $^{**}p \leq 0.01$, $^{***}p \leq 0.001$).

3.4. Cytocompatibility of Ca doped cit $EuPO_4$ nH_2O

The cytocompatibility of cit $EuPO_4$ nH_2O samples doped with different concentrations of Ca^{2+} was tested in a MTT assay on the GTL 16 human carcinoma cells and on the m17.ASC murine mes enchymal stem cells, after incubation at concentrations ranging from 0.1 to 100 µg/ml. No toxicity was observed on GTL 16 cells at any nanoparticle concentration (Fig. 9a), since in all cases full cell viability was observed. In the case of mesenchymal stem cells, low levels of Eu^{3+} were fully compatible with cell viability (Fig. 9b). However, if nanoparticles were doped with higher concentrations of Eu^{3+} a certain level of toxicity was observed. In these cases, the addition of doping Ca^{2+} in samples resulted in higher cell via bility in a dose response manner. In no case viability was lower than 70%, which is the cut offindicated by ISO 10993 5:2009 [64].

The different behavior of the two cell lines is not unexpected, since it is largely reported from the literature that cell lines can dif fer in their sensitivity to external stimuli [65,66] and indeed m17. ASC cells were already found to be less resistant than GTL 16 cells to the stress possibly induced by the presence of nanoparticles [39]. On the other side, both cell types were sensitive to the toxic activity of doxorubicin, which reduced their viability to less than 40%. This *in vitro* evaluation thus pointed out the good cytocompat ibility of the Ca doped cit $EuPO_4$ nH_2O nanoparticles.

4. Conclusions

This work was aimed to prepare luminescent $EuPO_4$ nH_2O nanophosphors doped with Ca^{2+} and coated with citrate since the presence of both components in the constitutive nanoparticles should be beneficial regarding the cytocompatibility that is required for bioimaging applications.

By applying the bioinspired crystallization route, consisting in thermal decomplexing of Ca^{2+}/Eu^{3+}/citrate/phosphate/carbonate solutions, we succeeded in preparing Ca doped citrate coated $EuPO_4$ nH_2O nanoparticles of the hexagonal rhabdophane phase. The general formula of this material, excluding citrate, is $Ca_{\alpha}Eu_{1-\alpha}(PO_4)_{1-\alpha}(HPO_4)_{\alpha}$ nH_2O, with αranging from 0 to 0.58 and n ~1. Their average dimensions (length and width) are below ~40 nm and ~8 nm respectively, and their aspect ratio decreases from 5.0 to 2.5 when the Ca^{2+} content increases, thus leading to more iso metric and irregular morphologies. Similar trend was found for the dimensions of the single crystal domains, whose coherent length and width are below ~13 and ~4 nm and the aspect ratio decreased from 3.6 to 1.1. In aqueous suspensions, these materials presented a low degree of aggregation below the median size (D_{50}), which become negligible below the percentile 10 (D_{10}), and very low ζ potential values (mostly between 3 and 0.5 mV) in the pH rage from 11 to 4.

Concerning the luminescence properties of these nanoparticles, neither the maturation time nor the concentration of doping agent affected significantly the excitation and emission wavelengths in solid state and aqueous suspensions. In solid state the observed excitation wavelengths were 319, 362, 379, 394 and 465 nm while the emission wavelengths were 577, 590, 614, 650 and 699 nm. In aqueous suspensions the maximum excitation wavelength observed was 230 nm and the emission wavelengths were 590, 616, 647 and 696 nm. In aqueous suspensions it was found that relative luminescence intensity (R.L.I.) is regulated by the Ca^{2+} level doping the structure, decreasing it by increasing the Ca^{2+} content (or decreasing Eu^{3+} amount) of the nanoparticles. Neither the pH (from 5 to 7.5) nor the ionic strength (from 0 to 100 mM NaCl), nor the temperature (from 25 to 37 °C) affected significantly the R.L.I.

This class of luminescent labeling agents is fully cytocompatible when in contact with GTL 16 cells (a human gastric carcinoma cell line) and shows an improved cytocompatibility as the Ca^{2+} content increases, when in contact with the more sensitive m17.ASC cell line (a spontaneously immortalized mouse mesenchymal stem cell clone from subcutaneous adipose tissue). On the basis of these analysis and the data reported by other authors regarding *in vivo* biocompatibility of Eu doped calcium phosphates nanoparticles [67,68], it is expected that also these Ca^{2} doped $EuPO_4$ nH_2O nanoparticles would be biocompatible *in vivo*. They can thus appear as promising new tailorable tools in view of biomedical applications as luminescent nanoprobes. As an example, they could also be the starting blocks to develop multifunctional nanoparti cles for efficient drug delivery, once coupled with therapeutic and targeting molecules [34].

Acknowledgments

We greatly acknowledge the project Biomin nanoapatite MAT2014 60533 R supported by Spanish MINEICO and co funded by FEDER and the Excellence Network of Crystallography and Crystallization "Factoría de Cristalización" FIS2015 71928 REDC supported by Spanish MINEICO. Cristóbal Verdugo Escamilla also acknowledges the Spanish MINEICO for his contract PTA2015 11103 I.

Appendix A. Supplementary material

Supplementary data to this article can be found online at https://doi.org/10.1016/j.jcis.2018.11.083.

References

[1] S. Chapman, M. Dobrovolskaia, K. Farahani, A. Goodwin, A. Joshi, H. Lee, T. Meade, M. Pomper, K. Ptak, J. Rao, R. Singh, S. Sridhar, S. Stern, A. Wang, J.B. Weaver, G. Woloschak, L. Yang, Nanoparticles for cancer imaging: The good, the bad, and the promise, Nano Today 8 (2013) 454–460.

[2] V.K.A. Sreenivasan, A.V. Zvyagin, E.M. Goldys, Luminescent nanoparticles and their applications in the life sciences, J. Phys.: Condens. Matter, 25 (2013) 194101 (23pp).

[3] D. Kim, J. Kim, Y. Il Park, N. Lee, T. Hyeon, Recent development of inorganic nanoparticles for biomedical imaging, ACS Cent. Sci. 4 (2018) 324–336.

[4] J. Li, J.-J. Zhu, Quantum dots for fluorescent biosensing and bio-imaging applications, Analyst 138 (2013) 2506–2515.

[5] C.-C. Fu, H.-Y. Lee, K. Chen, T.-S. Lim, H.-Y. Wu, P.-K. Lin, P.K. Wei, P.H. Tsao, H.-C. Chang, W. Fann, Characterization and application of single fluorescent nanodiamonds as cellular biomarkers, PNAS USA 104 (2007) 727–732.

[6] Y.-C. Yeh, B. Creran, V.M. Rotello, Gold nanoparticles: preparation, properties, and applications in bionanotechnology, Nanoscale 4 (2012) 1871–1880.

[7] F. Wang, W.B. Tan, Y. Zhang, X.P. Fan, M.Q. Wang, Luminescent nanomaterials for biological labelling, Nanotechnology 17 (2006) R1–R13.

[8] F. Oltolina, L. Gregoletto, D. Colangelo, J. Gómez-Morales, J.M. Delgado-López, M. Prat, Monoclonal antibody-targeted fluorescein-5-isothiocyanate-labeled biomimetic nanoapatites: a promising fluorescent probe for imaging applications, Langmuir 31 (2015) 1766–1775.

[9] A. Al-Kattan, V. Santran, P. Dufour, J. Dexpert-Ghys, C. Drouet, Novel contributions on luminescent apatite-based colloids intended for medical imaging, J. Biomater. Appl. 28 (5) (2014) 697–707.

[10] A. Al-Kattan, P. Dufour, J. Dexpert-Ghys, C. Drouet, Preparation and physicochemical characteristics of luminescent apatite-based colloids, J. Phys. Chem. C 114 (2010) 2918–2924.

[11] S. Padilla Mondéjar, A. Kovtuna, M. Epple, Lanthanide-doped calcium phosphate nanoparticles with high internal crystallinity and with a shell of DNA as fluorescent probes in cell experiments, J. Mater. Chem. 17 (2007) 4153–4159.

[12] Y.-P. Fang, A.-W. Xu, R.-Q. Song, H.-X. Zhang, L.-P. You, J.C. Yu, H.-Q. Liu, Systematic synthesis and characterization of single-crystal lanthanide orthophosphate nanowires, JACS 125 (2003) 16025–16034.

[13] Q. Luo, S. Shen, G. Lu, X. Xiao, D. Mao, Y. Wang, Synthesis of cubic ordered mesoporous YPO4:Ln^{3+} and their photoluminescence properties, J. Mater. Chem. 19 (2009) 8079–8085.

[14] F. Zhang, S.S. Wong, Ambient large-scale template-mediated synthesis of high-aspect ratio single-crystalline, chemically doped rare-earth phosphate nanowires for bioimaging, ACS Nano 4 (2010) 99–112.

[15] S.S. Syamchand, G. Sony, Europium enabled luminescent nanoparticles for biomedical applications, J. Lumin. 165 (2015) 190–215.

[16] H. Ito, Y. Fujishiro, T. Sato, A. Okuwaki, Preparation of lanthanide orthophosphates by homogeneous precipitation under hydrothermal conditions using lanthanide-EDTA chelates, Br. Ceram. Trans. 94 (1995) 146–150.

[17] R. Kijkowska, E. Cholewka, B. Duszak, X-ray diffraction and Ir-absorption characteristics of lanthanide orthophosphates obtained by crystallisation from phosphoric acid solution, J. Mater. Sci 38 (2003) 223–228.

[18] N. Clavier, R. Podor, N. Dacheux, Crystal chemistry of the monazite structure, J. Eur. Ceram. Soc. 31 (2011) 941–976.

[19] W. Bu, L. Zhang, Z. Hua, H. Chen, J. Shi, Synthesis and characterization of uniform spindle-shaped microarchitectures self-assembled from aligned single-crystalline nanowires of lanthanum phosphates, Cryst. Growth Des. 7 (2007) 2305–2309.

[20] Y.-P. Fang, A.-W. Xu, W.-F. Dong, Highly improved green photoluminescence from $CePO_4$:Tb/$LaPO_4$ core/shell nanowires, Small 1 (2005) 967–971.

[21] W. Bu, Z. Hua, H. Chen, J. Shi, Epitaxial synthesis of uniform cerium phosphate one-dimensional nanocable heterostructures with improved luminescence, J. Phys. Chem. B 109 (2005) 14461–14464.

[22] N.O. Nuñez, S.R. Liviano, M. Ocaña, J. Coll. Interf. Sci. 349 (2010) 484–491.

[23] C. Yu, M. Yu, C. Li, X. Liu, J. Yang, P. Yang, J. Lin, Citrate mediated synthesis of uniform monazite $LnPO_4$ (Ln = La, Ce) and Ln:$LaPO_4$ (Ln = Eu, Ce, Ce + Tb) spheres and their photoluminescence, J. Solid State Chem. 182 (2009) 339–342.

[24] X. Wang, M. Gao, Facile sonochemical synthesis and photoluminescent properties of lanthanide orthophosphate nanoparticles, J. Mater. Chem. 16 (2006) 1360–1365.

[25] Z. Hou, L. Wang, H. Lian, R. Chai, C. Zhang, Z. Cheng, J. Lin, Preparation and luminescence properties of Ce^{3+} and/or Tb^{3+} doped $LaPO_4$ nanofibers and microbelts by electrospinning, J. Solid State Chem. 182 (2009) 698–708.

[26] Y. Xing, M. Li, S.A. Davis, S. Mann, Synthesis and characterization of cerium phosphate nanowires in microemulsion reaction media, J. Phys. Chem. B 110 (2006) 1111–1113.

[27] X. Liu, Q. Wang, Z. Gao, J. Sun, J. Shen, Fabrication of lanthanide phosphate nanocrystals with well-controlled morphologies by layer-by-layer adsorption and reaction method at room temperature, Cryst. Growth & Des. 9 (8) (2009) 3707–3713.

[28] C. Zollfrank, H. Scheel, S. Brungs, P. Greil, Europium(III) Orthophosphates: synthesis, characterization, and optical properties, Cryst. Growth Des. 8 (3) (2008) 766–770.

[29] W. Di, X. Wang, P. Zhu, B. Chen, Energy transfer and heat-treatment effect of photoluminescence in Eu^{3+}-doped $TbPO_4$ nanowires, J. Solid State Chem. 180 (2007) 467–473.

[30] I.V. Tananaiev, Z. Vasilieva, Neorgan. Khim. (Russ) 9 (1964) 213.

[31] R. Kijkowska, Ca-substituted europium(III) phosphate monohydrate obtained through crystallisation from phosphoric acid solution, J. Alloys Comp. 363 (2004) 138–142.

[32] A. Al-Kattan, S. Girod-Fullan, C. Charvillat, H. Ternet-Fontebasso, P. Dufour, J. Dexpert-Ghys, V. Santran, J. Bordere, B. Pipy, J. Bernad, C. Drouet, Biomimetic nanocrystalline apatites: emerging perspectives in cancer diagnosis and treatment, Int. J. Pharm. 423 (2012) 26–36.

[33] J. Gómez-Morales, M. Iafisco, J.M. Delgado-López, S. Sarda, C. Drouet, Progress on the preparation of nanocrystalline apatites and surface characterization: overview of fundamental and applied aspects, Prog. Cryst. Growth Charact. Mater. 59 (2013) 1–46.

[34] M. Iafisco, J.M. Delgado-López, E.M. Varoni, A. Tampieri, L. Rimondini, J. Gómez-Morales, M. Prat, Cell surface receptor targeted biomimetic apatite nanocrystals for cancer therapy, Small 9 (2013) 3834–3844.

[35] M. Iafisco, M. Marchetti, J. Gómez Morales, M.A. Hernández-Hernández, J.M. García Ruiz, N. Roveri, Silica gel template for calcium phosphates crystallization, Cryst. Growth & Des. 9 (2009) 4912–4921.

[36] G.B. Ramírez-Rodríguez, J.M. Delgado López, J. Gómez-Morales, Evolution of calcium phosphate precipitation in hanging drop vapor diffusion by in situ Raman microspectroscopy, CrystEngComm 15 (2013) 2206–2212.

[37] J.M. Delgado-López, M. Iafisco, I. Rodríguez, M. Prat, J. Gómez-Morales, A. Tampieri, Crystallization of bioinspired citrate-functionalized nanoapatites with tailored carbonate content, Acta Biomaterialia 8 (2012) 3491–3499.

[38] F.J. Martínez-Casado, M. Iafisco, J.M. Delgado-López, C. Martínez-Benito, C. Ruiz-Pérez, D. Colangelo, F. Oltolina, M. Prat, J. Gómez-Morales, Bioinspired citrate–apatite nanocrystals doped with divalent transition metal ions, Cryst. Growth Des. 1 (2016) 145–153.

[39] J. Gómez-Morales, C. Verdugo-Escamilla, R. Fernández-Penas, C.M. Parra-Milla, C. Drouet, F. Maube-Bosc, F. Oltolina, M. Prat, J.F. Fernández-Sánchez, Luminescent biomimetic citrate-coated europium doped carbonated apatite nanoparticles for use in bioimaging: physico-chemistry and cytocompatibility, RSC Adv. 8 (5) (2018) 2385–2397.

[40] Y.Y. Hu, A. Rawal, K. Schmidt-Rohr, Strongly bound citrate stabilizes the apatite nanocrystals in bone, Proc. Natl. Acad. Sci. USA 107 (2010) 22425–22429.

[41] A.A. Coelho, TOPAS and TOPAS-Academic: an optimization program integrating computer algebra and crystallographic objects written in C++, J. Appl. Cryst. 51 (2018) 210–218.

[42] D. Ectors, F. Goetz-Neunhoeffer, J. Neubauer, A generalized geometric approach to anisotropic peak broadening due to domain morphology, J. Appl. Cryst. 48 (2015) 189–194.

[43] D. Ectors, F. Goetz-Neunhoeffer, J. Neubauer, Domain size anisotropy in the double-Voigt approach: an extended model, J. Appl. Cryst. 48 (2015) 1998–2001.

[44] C. Combes, R. Bareille, C. Rey, Calcium carbonate–calcium phosphate mixed cement compositions for bone reconstruction, J. Biomed. Mater. Res. Part A 79 (2006) 318–328.

[45] S. Lucas, E. Champion, D. Bernache-Assollant, G. Leroy, Rare earth phosphate powders $RePO_4{\cdot}nH_2O$ (Re=La, Ce or Y) II. Thermal behavior, J. Solid State Chem. 177 (4–5) (2004) 1312–1320.

[46] J. Cho, C.H. Kim, Solid-state phase transformation mechanism from hexagonal GdPO4:Eu^{3+} nanorods to monoclinic nanoparticles, RSC Adv. 4 (2014) 31385–31392.

[47] R. Kijkowska, Thermal decomposition of lanthanide orthophosphates synthesized through crystallisation from phosphoric acid solution, Thermochim. Acta 404 (2003) 81–88.

[48] M.T. Colomer, I. Delgado, A.L. Ortiz, J.C. Fariñas, Microwave-assisted hydrothermal synthesis of single-crystal nanorods of rhabdophane-type Sr-doped $LaPO_4.nH_2O$, J. Am. Ceram. Soc. 97 (3) (2014) 750–758.

[49] N. Kumar Sahu, R.S. Ningthoujam, D. Bahadur, Disappearance and recovery of luminescence in $GdPO_4$:Eu^{3+} nanorods: Propose to water/OH• release under near infrared and gamma irradiations, J. Appl. Phys. 112 (2012) 014306.

[50] G. Socrates, Infrared and raman characteristics group frequencies. tables and charts, 3rd ed., John Wiley and Sons Ltd, Chichester, 2001.

[51] P. Ivachenko, J.M. Delgado-López, M. Iafisco, J. Gómez-Morales, A. Tampieri, G. Martra, Y. Sakhno, On the surface effects of citrates on nano-apatites: evidence of a decreased hydrophilicity, Sci. Rep. 7 (2017) 8901.

[52] M. Sato, S. Matsuda, structure of vaterite and infrared spectra, Z. Kristallograph 129 (1969) 405–410.

[53] M. Lundqvist, J. Stigler, G. Elia, I. Lynch, T. Cedervall, K.A. Dawson, Nanoparticle size and surface properties determine the protein corona with possible implications for biological impacts, Proc. Natl. Acad. Sci. USA 105 (2008) 14265–14270.

[54] C.L. Mooney, X-ray diffraction study of cerium phosphate and related crystals. I. hexagonal modification, Acta Cryst. 3 (1950) 337–340.

[55] L. Veselinovic, L. Karanovic, Z. Stojanovic, I. Bračko, S. Markovic, N. Ignjatovic, D. Uskokovic, Crystal structure of cobalt-substituted calcium hydroxyapatite nanopowders prepared by hydrothermal processing, J. Appl. Crystallogr. 43 (2010) 320–327.

[56] I. Hemmilä, S. Dakubu, V.-M. Mukkala, H. Siitaria, T. Lövgrena, Europium as a label in time-resolved immunofluorometric assays, Anal. Biochem. 137 (1984) 335–343.

[57] F.S. Richardson, Terbium(III) and europium(III) ions as luminescent probes and stains for biomolecular systems, Chem. Revs. 82 (1982) 541–552.
[58] A. Al-Katan, V. Santran, P. Dufour, J. Dexpert-Ghys, C. Drouet, Novel contributions on luminescent apatite-based colloids intended for medical imaging, J. Biomater. Appl. 28 (2014) 697–707.
[59] W.T. Carnall, P.R. Fields, K. Rajnak, Electronic Energy Levels of the Trivalent Lanthanide Aquo Ions. III. Tb^{3+}, J. Chem. Phys. 49 (1968) 4424–4442.
[60] W.T. Carnall, P.R. Fields, K. Rajnak, Spectral intensities of the trivalent lanthanides and actinides in solution. II. Pm^{3+}, Sm^{3+}, Eu^{3+}, Gd^{3+}, Tb^{3+}, Dy^{3+}, and Ho^{3+}, J. Chem. Phys. 49 (1968) 4412–4423.
[61] J. Singh, J. Manam, Structural and spectroscopic behaviour of Eu^{3+}-doped $SrGd_2O_4$ modified by thermal treatments, J. Mater. Sci. 51 (2016) 2886–2901.
[62] J.R. Lakowicz, Principles of Fluorescence Spectroscopy, Third Edition., Springer, New York, USA, 2006.
[63] G.G. Guilbault, General aspects of luminescence spectroscopy, Practical Fluorescence, Marcel Dekker, New York, 1990.
[64] ISO 10993-5 Biological Evaluation of Medical Devices Part 5: Tests for In Vitro Cytotoxicity (International Standard Organization, Geneve, CH), 2009.
[65] M.I. Khan, A. Mohammad, G. Patil, S.A. Naqvi, L.K. Chauhan, I. Ahmad, Induction of ROS, mitochondrial damage and autophagy in lung epithelial cancer cells by iron oxide nanoparticles, Biomaterials 33 (2012) 1477–1488.
[66] M. Nedyalkova, B. Donkova, J. Romanova, G. Tzvetkov, S. Madurga, V. Simeonov, Iron oxide nanoparticles - in vivo/in vitro biomedical applications and in silico studies Adv, Coll. Interf. Sci. 249 (2017) 192–212.
[67] F. Chen, P. Huang, Y.J. Zhu, J. Wu, C.L. Zhang, D.X. Cui, The photoluminescence, drug delivery and imaging properties of multifunctional Eu^{3+}/Gd^{3+} dual-doped hydroxyapatite nanorods, Biomaterials 32 (2011) 9031–9039.
[68] C. Rosticher, B. Viana, T. Maldiney, C. Richard, C. Chanéac, Persistent luminescence of Eu, Mn, Dy doped calcium phosphates for in-vivo optical imaging, J Lumin. 70 (2016) 460–466.